nature communications

Article

https://doi.org/10.1038/s41467-025-64959-x

Nanofiller-confined spatial fluctuation in monomer diffusion synthesizing ultrafast reverse osmosis membranes driven by hydrogen-bonding networks

Received: 31 May 2025

Accepted: 29 September 2025

Published online: 13 November 2025

Check for updates

Ruoyun Lin[1,6], Qipeng Zhao[1,2,6], Huaqiang Chu[1,2] ✉, Fan Feng[3], Xuefei Zhou[1,2], Xu Jiang[4] ✉, Lu Shao[5] ✉ & Yalei Zhang[1,2] ✉

Thin-film composite (TFC) reverse osmosis (RO) membranes encounter a significant trade-off between water permeability and selectivity. This study presents a mechanism to address this limitation by altering the structure of the polyamide (PA) layer. By incorporating layered double hydroxides (LDH) and sodium lignosulfonate (SL), we establish differential diffusion resistances during interfacial polymerization (IP). This approach facilitates the diffusion of m-phenylenediamine (MPD) across the interface while concurrently inhibiting it in the bulk phase, thereby inducing spatial fluctuations in monomer diffusion. The resulting heterogeneous polymerization dynamics yield a thin, highly wrinkled PA layer that promotes ultrafast water transport. Moreover, the hydrophilic sulfonic groups ($-SO_3^-$) present on the LDH nanosheets form a robust hydrogen-bonding network with water, further enhancing transport efficiency. The optimized membrane attains a water permeance of 4.00 LMH·bar^{-1} and a NaCl rejection rate of 99.4%, surpassing most current TFC/TFN RO membranes. This research offers insights into the control of the polymerization process, contributing to the design of next-generation RO membranes.

The escalating global challenge of water scarcity necessitates the implementation of sustainable water resource management strategies to ensure a reliable supply of clean, safe, and sufficient water[1–3]. Among existing technologies, reverse osmosis (RO), a pressure-driven membrane process that operates without phase change, has emerged as a leading technology to address critical freshwater shortages, particularly through seawater desalination and wastewater reclamation[4–6]. Its widespread adoption is attributed to its relatively high energy efficiency and comparatively low carbon footprint[7]. Yet, despite decades of development, RO membrane performance remains constrained by an intrinsic trade-off, where enhancing water permeability typically comes at the cost of reduced solute selectivity[8,9].

Thin-film composite (TFC) membranes, which are quintessential representatives of RO membranes, are widely employed for water filtration due to their cost-effectiveness, operational simplicity, and scalability for industrial applications[10]. Nevertheless, a persistent

[1]State Key Laboratory of Water Pollution Control and Green Resources Recycling, College of Environmental Science and Engineering, Tongji University, Shanghai, China. [2]Shanghai Institute of Pollution Control and Ecological Security, Tongji University, Shanghai, China. [3]Department of Chemical and Biomolecular Engineering, National University of Singapore, Singapore, Singapore. [4]Advanced Membranes and Porous Materials Center, Division of Physical Science and Engineering, King Abdullah University of Science and Technology (KAUST), Thuwal, Saudi Arabia. [5]State Key Laboratory of Urban Water Resource and Environment, School of Chemistry and Chemical Engineering, Harbin Institute of Technology, Harbin, China. [6]These authors contributed equally: Ruoyun Lin, Qipeng Zhao. ✉e-mail: chuhuaqiang@tongji.edu.cn; xu.jiang@kaust.edu.sa; shaolu@hit.edu.cn; zhangyalei@tongji.edu.cn

trade-off between permeability and selectivity remains a critical constraint limiting their performance. A key strategy in pursuing ultrafast water transport in TFC membranes involves creating thin polyamide (PA) active layers to minimize the transport distance for water molecules. Traditional TFC membranes are fabricated through interfacial polymerization (IP) reactions between aqueous-phase m-phenylenediamine (MPD) and organic-phase trimesoyl chloride (TMC) at the aqueous-organic interface[11]. The growth of the PA layer is generally considered a diffusion-controlled process[12], critically governed by the diffusion rate of the amine monomer to the reaction zone[13,14].

In recent years, numerous strategies have been developed to modulate this diffusion, including low-temperature polymerization[15–17], incorporation of intermediate layers[18–20], and 3D printing[21–23]. However, these approaches often suffer from high costs and complex manufacturing procedures. As an alternative, low-cost and process-compatible nanofillers have recently garnered considerable attention[24–31]. For instance, chitosan-based nanoparticles have been shown to modulate the monomer diffusion and result in a thinner PA layer, improving permeability without sacrificing selectivity[32]. Notably, compared to zero-dimensional (0D), one-dimensional (1D), and three-dimensional (3D) nanofillers, two-dimensional (2D) nanofillers, due to their larger lateral dimensions and high aspect ratio, can effectively unfold at the aqueous-organic interface, promoting better control over the interfacial behavior of the amine monomer[33]. Furthermore, the ultra-thin thickness and interlayer pathways formed by stacking 2D nanofillers lower the permeation resistance of thin-film nanocomposite (TFN) membranes[34]. Layered double hydroxides (LDH), a class of synthetic nanoclays composed of two-dimensional positively charged hydroxide layers paired with counter anions, offer significant advantages, including low cost, ease of preparation, and environmental sustainability[35]. Their distinctive layered structure has been shown to modulate the IP process, inhibiting PA growth and promoting the formation of a thinner active layer; however, the precise underlying mechanisms require further investigation[36].

Moreover, recent studies have revealed that the separation performance is not solely dictated by thickness, but also critically by its molecular-scale heterogeneity and surface topology[33]. While inhibiting MPD diffusion can yield a thinner and smoother selective layer[18,37,38], substantial experimental evidence has demonstrated that nanoscale heterogeneity, such as surface wrinkling and microstructural diversity, also plays a vital role in enhancing water transport, potentially facilitating ultrafast permeation[1,2,39,40]. For example, lignin and its derivative, sodium lignosulfonate (SL), have been shown to promote the cross-interface diffusion of MPD, thereby increasing the surface irregularity. Coupled with abundant hydrophilic functional groups (i.e., hydroxyl or −OH, and sulfonic or $-SO_3^-$), which can establish extensive hydrogen-bonding networks, the resulting membrane exhibits significantly enhanced permeability[41–43]. Collectively, these give rise to an inhibition-promotion paradox concerning amine monomer diffusion, underscoring the necessity of achieving a delicate balance to achieve both desirable thickness and optimal morphology.

In this study, we report a mechanism to strategically regulate the structure and surface topology of the PA selective layer, thus enabling exceptional separation performance in RO membranes. By leveraging the synergistic effects of LDH and SL, we establish a route to precisely control the overall structure and surface morphology of the PA layer by spatially manipulating MPD diffusion pathways. This enables a delicate balance within the inhibition-promotion paradox of MPD diffusion, allowing for ultrafast water permeation while maintaining satisfactory solute selectivity. The strategy introduces differential diffusion resistances, retarding bulk-phase transport while promoting cross-interface MPD diffusion, thereby inducing spatial fluctuations in monomer diffusion rates and fluxes. These fluctuations lead to heterogeneous polymerization dynamics, resulting in the formation of a thin and highly wrinkled PA layer. This breakthrough not only resolves the inhibition-promotion paradox but also presents a robust, scalable and cost-effective method to engineer a PA selective layer, making a significant advancement over current state-of-the-art approaches. This work provides insights into the kinetic control of the IP process, opening avenues for next-generation RO membrane design in water treatment.

Results

Fabrication and characterization of LDH-SL TFN membranes

The crystal structure of the as-synthesized LDH and sodium lignosulfonate-modified LDH (LDH-SL) was analyzed using X-ray diffraction (XRD), as shown in Fig. 1a and Supplementary Fig. 1. All samples exhibited characteristic diffraction patterns of a typical LDH structure (JCPDS No. 35-0964). Distinct and narrow diffraction peaks were observed around 11° and 22°, corresponding to the (003) and (006) planes, respectively, indicating an interlayer spacing of 7.5 Å. This suggests that no additional compensating anions or molecules were intercalated into the interlayer space during surface modifications[44], which is significantly larger than the water molecule size (approximately 2.8 Å), thus supporting the potential for ultrafast water transport. Transmission electron microscopy (TEM) images clearly depicted the morphological structure before and after modification (Fig. 1b, c and Supplementary Fig. 2). Both the as-synthesized LDH and LDH-SL exhibited a typical plate-like structure[45], with lateral dimensions ranging from 41.17 to 42.40 nm. The interplanar spacings between adjacent host layers were measured to be 0.73 and 0.74 nm for the (003) planes, consistent with the XRD results. Fourier transform infrared (FTIR) spectroscopy was employed to analyze the chemical composition of LDH-SL (Fig. 1d and Supplementary Fig. 3). The spectra revealed characteristic peaks associated with specific functional groups. Notably, the absorption band at 3448 cm^{-1} was assigned to O–H bond stretching vibrations originating from the metal octahedral structures[46]. While the absorption band at 1361 cm^{-1} was attributed to the asymmetric stretching vibrations of C=O bonds in CO_3^{2-} ions[47]. The absorption peaks between 400 and 800 cm^{-1} corresponded to lattice vibrations of the metal-oxygen bonds[48]. Following SL modification, three new peaks merged at 1510, 1207, and 1041 cm^{-1}, corresponding to the stretching vibrations of the aromatic skeleton, bending vibrations of the guaiacyl unit, and S=O symmetric stretching of the SL moiety, respectively[49]. These spectral features collectively confirm the successful functionalization and synthesis of LDH-SL.

A highly permeable PA film anticipated by researchers necessitates the fabrication of a thin selective layer featuring a distinctive ridge-and-valley morphology on the membrane surface[50,51]. As shown in the scanning electron microscopy (SEM) images (Fig. 1e, h), the pristine TFC membrane and 2LDH-1SL TFN membrane exhibited markedly different surface morphologies. The notation 2LDH-1SL denotes the mass ratio of LDH to SL employed during nanofiller synthesis, a parameter that we have identified as critical for controlling membrane structure. The former displayed typically mild PA wrinkles, whereas the latter exhibited a more pronounced ridge-and-valley structure, potentially increasing the effective filtration area, thereby enhancing membrane permeability. Energy dispersive spectroscopy (EDS) analysis confirms the uniform distribution of aluminum (Al) and magnesium (Mg) across the PA layer surface (Supplementary Fig. 4), validating the successful incorporation of 2LDH-1SL within the selective layer. Atomic force microscopy (AFM) analysis further corroborated this difference in surface morphology (Fig. 1f, i). Despite the root mean square roughness (RMS) of the 2LDH-1SL TFN membrane being comparable to that of the TFC membrane, the average height of the ridge-and-valley features is significantly greater, approximately 454 nm compared to 393 nm for conventional PA wrinkles. It is important to clarify that while RMS roughness provides a general measure of surface height variations, it does not fully capture the amplitude of specific topographical features. A more detailed analysis

https://doi.org/10.1038/s41467-025-64959-x

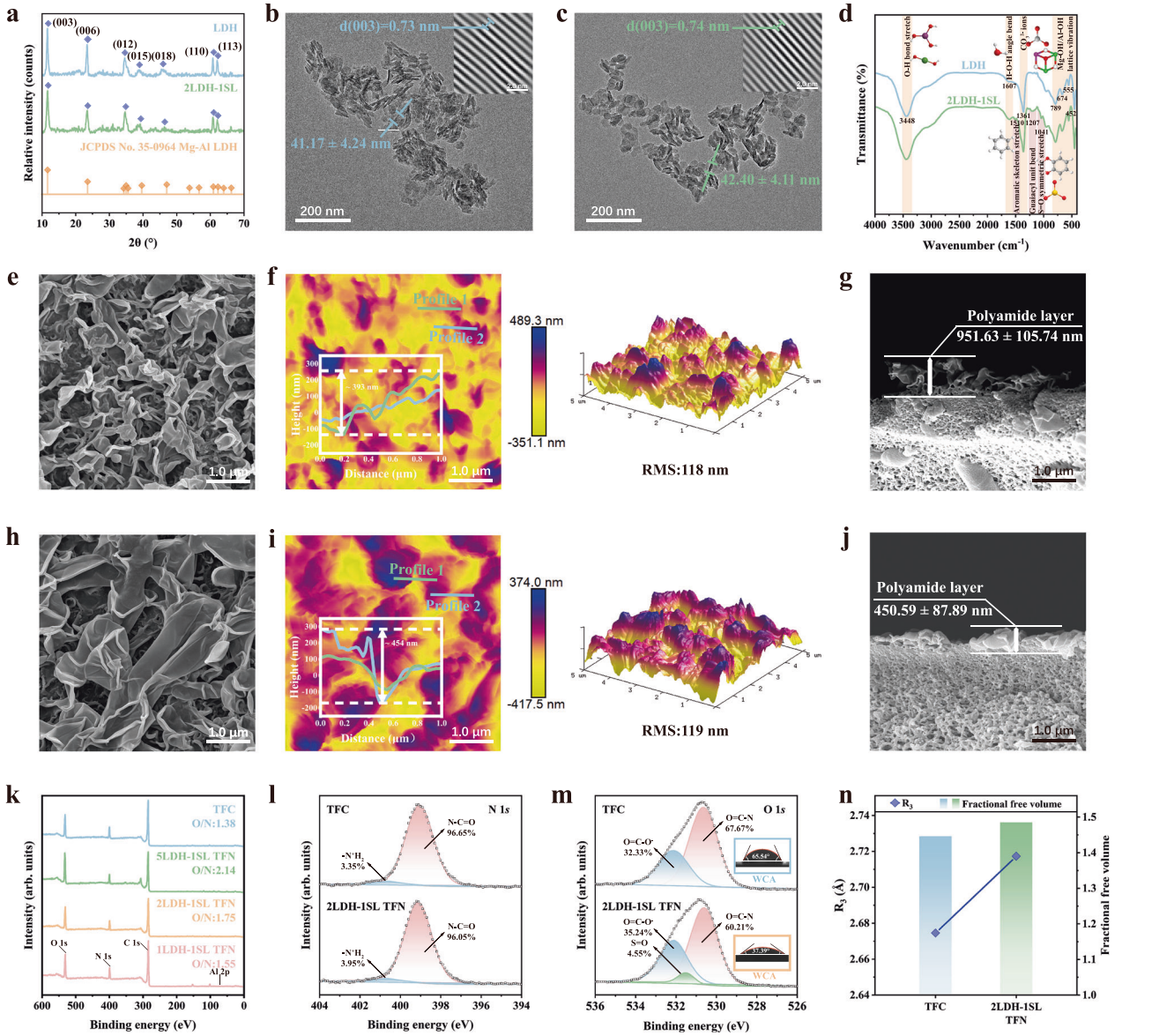

Fig. 1 | In-depth spectroscopic and morphological examination of sodium lignosulfonate-modified layered double hydroxides (LDH-SL) nanoparticles and LDH-SL thin-film nanocomposite (TFN) membranes. a X-ray diffraction (XRD) pattern illustrating the crystalline phases. Transmission electron microscopy (TEM) images of **b** LDH and **c** 2LDH-1SL depicting the morphological structure. **d** Fourier transform infrared (FTIR) spectrum validating the presence of functional groups. Scanning electron microscopy (SEM) images of **e** thin-film composite (TFC) and **h** 2LDH-1SL TFN membranes showcasing the surface morphology of the membranes. Atomic force microscopy (AFM) images, as well as root mean square roughness (RMS) measurements for **f** TFC and **i** 2LDH-1SL TFN membranes, represent their surface roughness characteristics. Cross-sectional SEM images of **g** TFC and **j** 2LDH-1SL TFN membranes accentuating the membranes' thickness. **k** X-ray photoelectron spectroscopy (XPS) spectra, accompanied by high-resolution **l** N 1*s* and **m** O 1*s* spectra highlighting the elemental composition (inserted water contact angles (WCAs) illustrating hydrophilicity). **n** Positron annihilation lifetime spectroscopy (PALS) underscoring the fractional free volume (FFV) and pore size (R_3) of the membranes.

using height distribution histograms (Supplementary Fig. 6) confirms that the 2LDH-1SL TFN membrane possesses significantly greater peak-to-valley distances, which directly contribute to an increased effective surface area for water transport. This disparity is attributed to the role of LDH-SL in modulating MPD diffusion at the aqueous-organic interface. By creating localized free energy minima, LDH-SL accelerates the reaction rate between MPD and TMC, substantially increasing interfacial instability. Interestingly, cross-sectional SEM images reveal that the PA layer of the 2LDH-1SL TFN membrane is notably thinner than that of the pristine TFC membrane, with a significant thickness reduction from 951.63 to 450.59 nm (Fig. 1g, j). This observation suggests an opposite mechanism that LDH-SL may also suppress MPD diffusion in the organic bulk phase through steric hindrance, thereby limiting polymerization and resulting in a thinner PA layer. By meticulously balancing the interplay between the contradictory inhibition-promotion of MPD diffusion, a highly wrinkled TFN membrane was successfully fabricated, offering enhanced transport pathways and shortened transmission distances for water molecules[52]. The amphiphilic nature of SL was substantiated as the key factor governing this balance (Supplementary Fig. 7). At lower SL doping ratios (i.e., SL to LDH), the impeded diffusion of MPD within the organic bulk phase by nanofillers predominates during membrane formation, resulting in a smooth, thin PA layer. In contrast, at higher SL doping ratios, the interfacial diffusion of MPD is enhanced, leading to a rougher and thicker PA morphology. The specific role of LDH-SL in regulating PA nanofilm formation will be further elaborated in the following sections.

X-ray photoelectron spectroscopy (XPS) was utilized to characterize the elemental composition of the membrane surfaces. Based on the O/N ratio, it was determined that the modified TFN membranes incorporating nanoparticles exhibited a lower degree of network cross-linking compared to the nascent TFC membranes (Fig. 1k and Supplementary Table 1)[53]. While this ratio provides a useful preliminary indication, we acknowledge that the oxygen-rich LDH-SL nanofiller could contribute to the total oxygen signal, potentially inflating the O/N ratio. Therefore, stronger evidence for reduced cross-linking is derived from high-resolution spectra and positron annihilation lifetime spectroscopy (PALS) data. This reduction in cross-linking is attributed to the presence of nanoparticles dispersed within the organic bulk phase, which hinders the mass transfer of MPD, thereby disrupting the IP process. To further elucidate the chemical states of the membrane's surface compositions, high-resolution N 1*s* and O 1*s* XPS spectra were analyzed (Fig. 1l, m). In comparison to the TFC membrane, the 2LDH-1SL TFN membrane exhibited a decreased proportion of amide bonds (N–C=O/O=C–N), while the ratio of unreacted amino groups ($-NH_2$) increased, correlating with the reduction in network cross-linking. PALS further corroborated this conclusion (Fig. 1n and Supplementary Table 3), revealing an increase in both the fractional free volume (FFV) and the average pore radius (R_3) of the 2LDH-1SL TFN membrane. This indicates an increase in the size and/or number density of free volume elements within the polymer matrix, providing additional diffusion pathways for water molecules and enhancing permeability[54,55]. Additionally, following the incorporation of SL, there was a significant alteration in the relative abundance of S=O and carboxyl groups ($O=C-O^-$) within the 2LDH-1SL TFN membrane. Surface wettability tests demonstrated a notable improvement in hydrophilicity, with water contact angles (WCA) decreasing from 65.54° for the TFC membrane to 37.39° for the 2LDH-1SL TFN membrane (insert in Fig. 1m). The notable enhancement in hydrophilicity can be ascribed not only to the increased number of water molecular pathways, but also to the introduction of supplementary hydrophilic functional groups via SL modification.

Regulating mechanisms of LDH-SL on the PA nanofilm formation

The hydrophilic $-SO_3^-$ and carboxylate ($-COO^-$) groups in SL molecules can form strong hydrogen bonds with water molecules, while the hydrophobic benzene ring structure exhibits considerable affinity for *n*-hexane, demonstrating typical surfactant behavior. By precisely controlling the doping ratio of SL to LDH, the interfacial behavior of the system can be spatially manipulated: LDH-SL nanoparticles partially accumulate at the aqueous-organic interface and partially disperse in the organic bulk phase (Fig. 2a, e). The thermodynamics governing this partitioning are dictated by the amphiphilic nature of the SL-modified nanofillers. The SL:LDH ratio directly controls the surface energy of the nanoparticles. At lower ratios, the particles remain relatively hydrophobic and preferentially disperse in the organic bulk phase to minimize interfacial energy. As the SL ratio increases, the enhanced hydrophilicity and amphiphilicity lower the free energy penalty associated with residing at the aqueous-organic interface, promoting their accumulation there. Direct characterization through cross-sectional SEM-EDS mapping ultimately confirms this spatial arrangement (Supplementary Fig. 12). Molecular dynamics (MD) simulation results reveal that MPD molecules preferentially reside in the aqueous-organic interface region with the lowest free energy (Fig. 2b). This phenomenon is attributed to the amphiphilic nature of MPD, which consists of hydrophilic amine groups and hydrophobic benzene rings. The interfacial transport of MPD is consistently accompanied by a forward energy loss of approximately 41.46 kJ mol^{-1} (at 25 °C), indicating that, without continuous MPD consumption in the n-hexane phase for maintaining a concentration gradient, sustaining this transport across the interface is challenging.

The introduction of LDH-SL nanoparticles significantly alters the free energy landscape for MPD diffusion at the interface. Although the overall energy loss during MPD transfer to the n-hexane phase remains relatively unchanged, the accumulation behavior of LDH-SL at the interface induces multiple local minima in the free energy profile, forming an unconventional zigzag pattern (Fig. 2c). These local free energy minima create transition states with relatively low energy loss, allowing MPD to more easily overcome the energy barriers between adjacent extreme points, thus significantly enhancing the interfacial migration efficiency of MPD. Furthermore, this zigzag profile suggests a synergistic interfacial concentration effect; these local energy minima can act as temporary binding sites or traps for MPD molecules, increasing their local concentration and residence time at the interface. This, in turn, accelerates the polymerization reaction with TMC, further promoting the interfacial instability that leads to wrinkling.

As the SL doping ratio increases, the amphiphilic characteristics become more pronounced, promoting the enrichment of LDH-SL nanoparticles at the interface. This accumulation leads to a marked reduction in interfacial tension (Fig. 2d). Literature reports indicate that reduced interfacial tension can effectively lower the energy barrier for molecular diffusion from the aqueous to the organic phase[41]. This reduction in interfacial tension can also induce hydrodynamic instabilities (e.g., the Marangoni effect), which further contribute to the formation of highly wrinkled surface morphology. The zigzag free energy profile may stem from the dimensional match between the LDH interlayer spacing (approximately 7.5 Å, Fig. 1a) and the MPD molecule size (approximately 7.4 Å), as well as the periodic arrangement of hydrophilic and hydrophobic groups of LDH-SL along the transport direction[24]. It is noteworthy that the intermolecular attraction between the amine group of MPD and the $-COO^-$ group of LDH-SL reduces the system's free energy, while the repulsion between the amine group and the benzene ring increases the free energy.

In situ monitoring of MPD diffusion rates in quartz cuvettes via UV–Vis spectrophotometry (Fig. 2g) shows strong agreement with simulation data: as the enrichment of LDH-SL nanoparticles at the interface increases, the diffusion rate of MPD gradually improves (Fig. 2h). This phenomenon significantly enhances the effective availability of MPD monomers in the *n*-hexane phase, accelerating their polymerization reaction rate with TMC, consequently, leading to greater interface instability and promoting the formation of a highly wrinkled selective layer. This morphological feature substantially enlarges the effective permeation area of the membrane, demonstrating a significant advantage in enhancing water flux[56].

Furthermore, the diffusion behavior of MPD monomers in the organic bulk phase was thoroughly investigated. According to diffusion kinetics theory, the slope of the mean square displacement (MSD) curve positively correlates with diffusion rate[18]. As illustrated in Fig. 2f, the comparable size of MPD molecules and LDH interlayer spacing hinders MPD from traversing through the channels between LDH layers. The spatial confinement effect notably impedes the diffusion of MPD molecules. Based on the MSD curve in the Z-direction, the diffusion coefficient of MPD was calculated (Supplementary Fig. 13). Quantitative analysis indicates that in the system devoid of LDH-SL nanoparticles, the diffusion coefficient of MPD molecules is measured at $2.23(\pm0.35) \times 10^{-5}$ cm^2 s^{-1}; conversely, in the presence of LDH-SL nanoparticles, the diffusion coefficient significantly decreases to $1.59(\pm0.29) \times 10^{-5}$ cm^2 s^{-1}. The results from UV–Vis spectroscopic analysis also corroborate the substantial attenuation of MPD diffusion (Fig. 2i). Ultimately, the dispersion of LDH-SL nanoparticles within the organic bulk phase governs the diffusion dynamics of MPD molecules through the newly formed PA layer, contributing to a thinner PA membrane structure. This reduction in membrane thickness effectively shortens the transport pathway for water molecules, resulting in enhanced membrane permeability[57].

https://doi.org/10.1038/s41467-025-64959-x

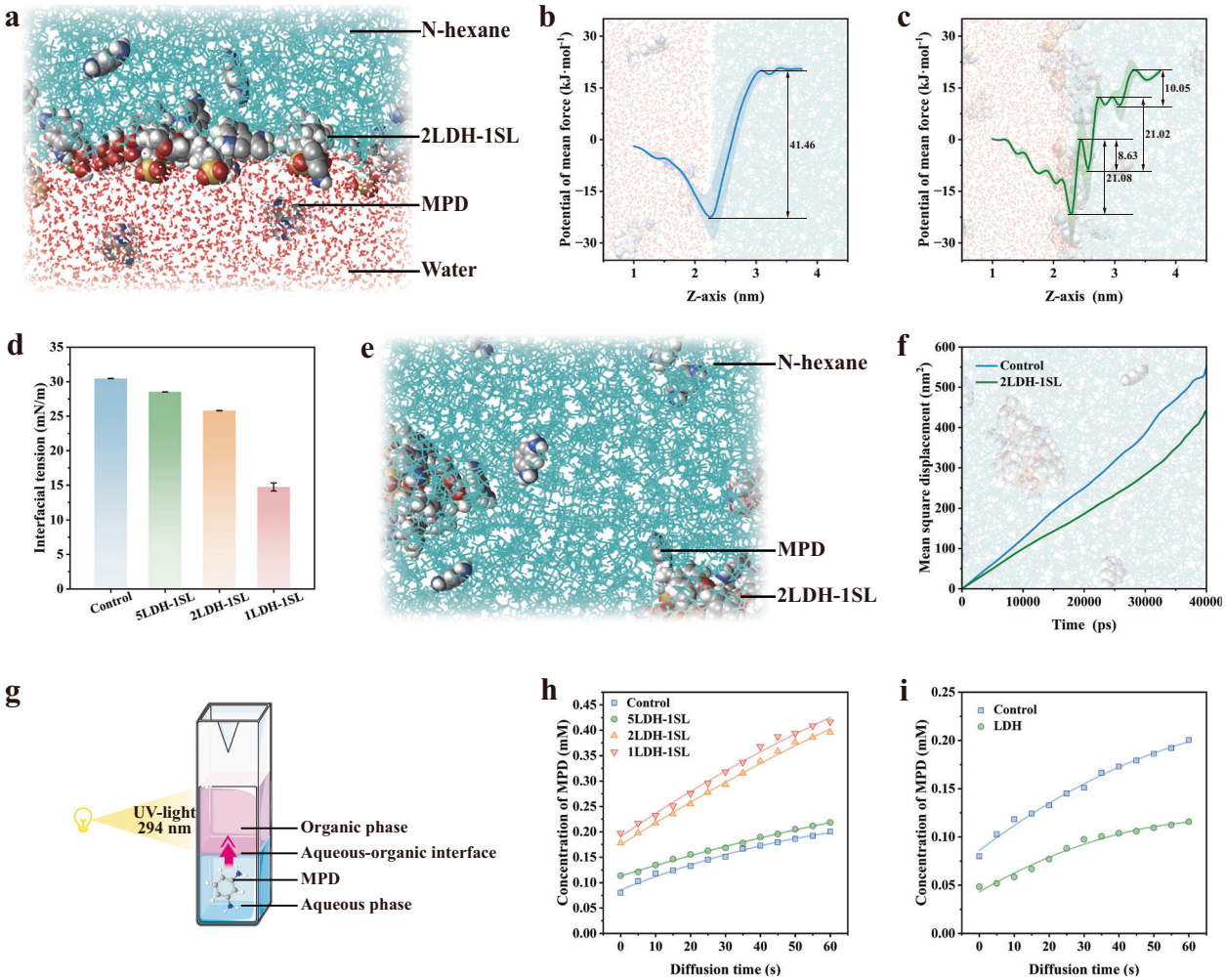

Fig. 2 | Mechanisms governing the incorporation of sodium lignosulfonate-modified layered double hydroxides (LDH-SL) nanoparticles in the fabrication of thin-film nanocomposite (TFN) membranes. a Molecular dynamics (MD) simulation of the aqueous-organic interface of n-hexane with 2LDH-1SL. The potential of mean force (PMF) of m-phenylenediamine (MPD) as a function of the z coordinates, perpendicular to the aqueous-organic interface: **b** without and **c** with 2LDH-1SL. The shaded regions indicate the standard deviation estimated over the simulation trajectory. **d** Interfacial tension between the MPD aqueous solution and n-hexane, with and without the addition of nanoparticles. Data are presented as mean values, with error bars representing the standard deviation from three independent measurements. **e** MD simulation of the organic bulk phase of n-hexane with 2LDH-1SL. **f** Mean square displacement (MSD) of MPD in the organic bulk phase, with and without 2LDH-1SL. **g** Schematic representation of the quantitative method employed to assess the diffusion extent of MPD from the aqueous phase to the organic phase. **h**, **i** MPD concentration in n-hexane over the reaction time during the interfacial polymerization (IP) process with and without the incorporation of nanoparticles. The cuvette illustration in (**g**) is adapted from Servier Medical Art, licensed under a Creative Commons Attribution 3.0 Unported License.

In summary, the fabrication of highly wrinkled TFN membranes is intricately associated with the dynamic equilibrium between the facilitated diffusion of MPD at the aqueous-organic interface and its inhibited diffusion within the organic bulk phase. This equilibrium process is substantially regulated by the amphiphilic nature of SL: at lower concentrations of SL, nanoparticles predominantly distribute within the organic phase, where steric hindrance impedes the mass transfer of MPD. This restriction significantly reduces the interfacial reaction kinetics with TMC, stabilizing the interface and favoring the development of a smooth, thin PA layer. Conversely, as SL concentration escalates, the directional enrichment of nanoparticles at the aqueous-organic interface generates localized minima in free energy, which thermodynamically favors the transport of MPD across the interface, subsequently resulting in the formation of a PA layer characterized by increased surface roughness and thickness. An optimal balance between these two contrasting mechanisms enables the precise modulation of IP dynamics with an ideal doping ratio of SL, ultimately facilitating the controlled fabrication of highly wrinkled TFN membranes with enhanced structural and transport properties (Fig. 3).

Separation performance of LDH-SL TFN membranes

The impact of varying SL doping ratios on the separation performance of LDH-SL TFN membranes was evaluated, as depicted in Fig. 4a. In comparison to the conventional TFC membrane, all LDH-SL TFN membranes, with an identical nanofiller loading of 0.10 wt%, exhibited enhanced water permeance. Among them, the 2LDH-1SL TFN membrane demonstrated the highest water permeance of 4.00 LMH bar^{-1}, which is 1.83 times greater than that of the conventional TFC membrane. SEM analysis revealed that all LDH-SL TFN membranes possessed a ridge-and-valley structure. Notably, the surface of the 2LDH-1SL TFN membrane was characterized by a more abundant and uniformly distributed structure (as shown in Fig. 1e, h, and Supplementary Fig. 7). According to Tang et al., nanoscale voids within such ridge-and-valley architecture can simultaneously increase the filtration surface area and optimize transport pathways, potentially enhancing water

https://doi.org/10.1038/s41467-025-64959-x

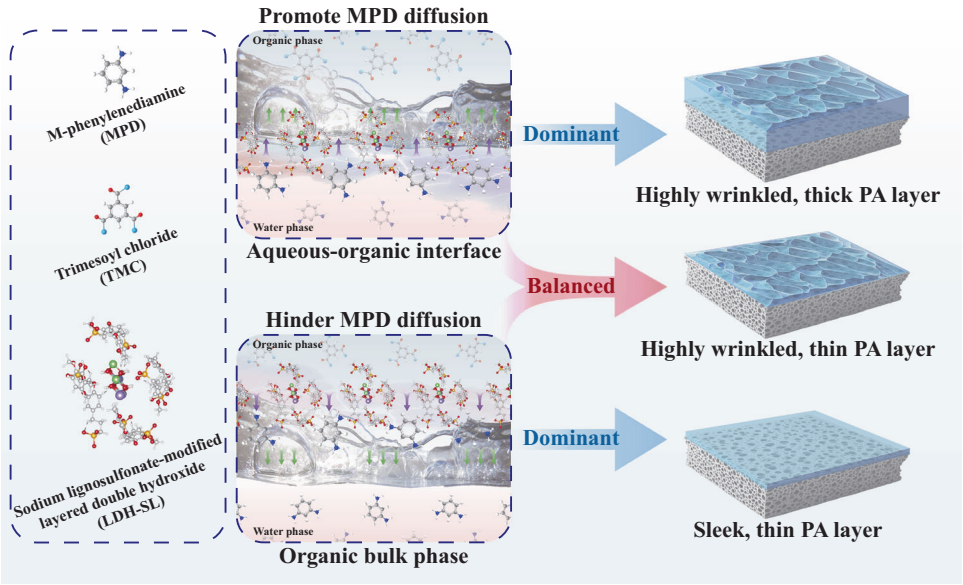

Fig. 3 | Mechanism of sodium lignosulfonate-modified layered double hydroxides (LDH-SL) in polyamide (PA) layer formation. Schematic illustration depicting the variability caused by dosage in the incorporation of LDH-SL nanoparticles during the fabrication of the PA layer.

permeance by one to two orders of magnitude[58]. Additionally, a reduced intrinsic thickness of the active layer further contributes to minimizing water transport resistance (Fig. 1i)[59]. In contrast, increasing the SL doping ratio beyond optimal levels resulted in a pronounced stacking of the PA layer, hindering water molecular transport and correlating with a slight decrease in observed water permeance. Despite this, the 2LDH-1SL TFN membrane still delivered high salt rejection, breaking through the traditional trade-off between permeability and selectivity. The presence of $-SO_3^-$ groups on the membrane surface imparted a stronger negative charge, theoretically enhancing electrostatic repulsion of Cl^- ions while facilitating Na^+ adsorption. Simultaneously, the well-defined pore structure of the 2LDH-1SL TFN membrane ensured high selectivity by allowing water molecules to pass through, while effectively excluding larger NaCl ions.

Building upon these findings, the optimal dosage of 2LDH-1SL nanoparticles was further investigated (Fig. 4b). As the concentration of 2LDH-1SL nanoparticles increased from 0 to 0.10 wt%, a substantial improvement in water permeance was observed, while maintaining a high salt rejection rate exceeding 99%. Beyond 0.10 wt%, no further enhancements were noted. This performance plateau is likely due to excessive nanoparticle accumulation within the PA layer, which increased its thickness, extended the water transport path, and heightened tortuosity within the dense structure, ultimately limiting further improvements in water permeance (Supplementary Fig. 8)[60]. Balancing separation performance with economic feasibility, the 0.10 wt% 2LDH-1SL TFN membrane (denoted as 2LDH-1SL TFN membrane) was selected for subsequent studies and referred to as the optimal configuration.

Further exploration was conducted regarding the contributions of LDH, lignin, and SL to the enhanced membrane separation performance, as illustrated in Fig. 4c. During the IP process, the steric hindrance introduced by LDH interfered with the mass transfer of MPD, which inhibited the growth of PA, resulting in a relatively looser selective layer. This structural change facilitated the diffusion of water molecules and enhanced water permeance by approximately 1.40 times. The incorporation of lignin stimulated the diffusion of MPD across the aqueous-organic interface and promoted the development of a well-distributed ridge-and-valley structure, further increasing water permeance to 1.73 times, closely mirroring the earlier contribution. Following the substitution of lignin with SL, the introduction of hydrophilic $-SO_3^-$ functional groups further enhanced the interaction between the PA layer and water molecules, thereby facilitating ultrafast water transport. To better understand the relative contributions of enhanced surface area versus intrinsic transport properties, we conducted an analysis to decouple these effects. By estimating the surface area enhancement from AFM data, we calculated an area-normalized intrinsic flux (Supplementary Section 1.5). The results indicate that while increased surface area is a significant factor, the intrinsic flux of the 2LDH-1SL TFN membrane remains substantially higher than that of the control, confirming the critical role of enhanced hydrophilicity and the formation of hydrogen-bonding networks in facilitating water transport.

Moreover, the 2LDH-1SL TFN membrane exhibited structural durability and long-term stability over an extended filtration duration of 72 h (Fig. 4d), maintaining a NaCl rejection rate consistently above 99% and achieving a steady average water permeance of 3.91 LMH bar^{-1}. The performance of the 2LDH-1SL TFN membrane surpassed previously reported TFC/TFN RO membranes, stepping across the boundary line of conventional selectivity-permeability trade-off. Specifically, it demonstrated either the highest water/NaCl selectivity at a given water permeance or the highest water permeance at specified water/NaCl selectivity levels, highlighting its superior separation performance (Fig. 4e).

Regulatory mechanisms of LDH-SL on facilitated water permeation

The permeation behavior of water molecules within the selective layer is predominantly governed by the synergistic regulation of its structural and chemical properties. During this process, water molecules must overcome a specific energy barrier associated with solvation and diffusion. While previous sections have systematically discussed the structural design optimizations that facilitate ultrafast water transport, the intermolecular interactions between water molecules and functional groups in the PA network also play a crucial role in determining permeation flux. Although it has been established that the introduction of SL markedly enhances the hydrophilicity of the TFN membrane surface, as illustrated in Supplementary Fig. 10, MD simulations were employed to further elucidate the underlying diffusion mechanism of water molecules within the PA selective layer. Specifically, the simulations focused on analyzing the binding characteristics between water

https://doi.org/10.1038/s41467-025-64959-x

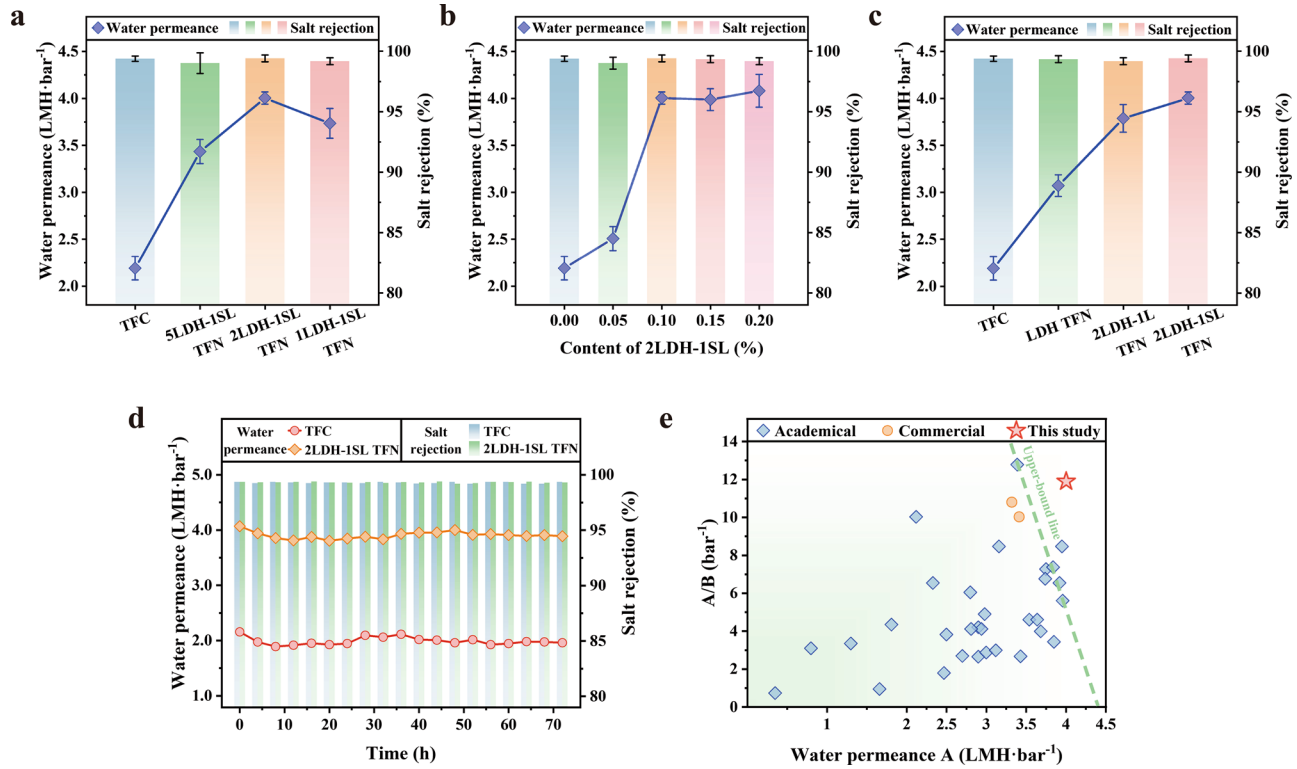

Fig. 4 | Separation performance of various membranes. a The impact of the sodium lignosulfonate (SL) doping ratio on the water permeance and salt rejection of SL-modified layered double hydroxides (LDH-SL) thin-film nanocomposite (TFN) membranes. **b** The influence of 2LDH-1SL nanoparticle dosage on the water permeance and salt rejection of LDH-SL TFN membranes. **c** The contributions of LDH (LDH TFN), lignin (LDH-L TFN), and SL (LDH-SL TFN) to the enhanced membrane separation performance. **d** Long-term separation performance of conventional TFC membrane and 2LDH-1SL TFN membrane. **e** A comprehensive comparison of water permeance and water/NaCl selectivity (A/B) between the 2LDH-1SL TFN membrane and the state-of-the-art thin-film composite (TFC)/TFN reverse osmosis (RO) membranes reported in the literature (detailed water permeance and salt rejection data are provided in Supplementary Table 4). Data are presented as mean values, with error bars representing the standard deviation from three independent measurements.

molecules and representative molecular fragments: (I) amide groups, (II) LDH, and (III) $-SO_3^-$ groups (Fig. 5a).

The calculated non-bonded interaction energy (IE) results reveal that the interaction strength follows the trend of |IEIII| > |IEII| > |IEI| (Fig. 5b), indicating that $-SO_3^-$ groups exhibit the strongest affinity for water molecules, followed by LDH and amide groups. Notably, the LDH-SL modification introduces both LDH and $-SO_3^-$ functionalities, which substantially enhance the interaction with water molecules. In particular, the electrostatic interaction energy between water molecules and $-SO_3^-$ groups was found to reach as high as 7729.37 kJ mol^{-1} (Fig. 5c and Supplementary Fig. 17). According to literature, a significant Mulliken electron transfer phenomenon exists between $-SO_3^-$ groups and water molecules, contributing to the formation of a robust hydrogen-bonding network that plays a critical role in electrostatic interactions[60]. This finding suggests that the incorporation of $-SO_3^-$ groups establishes a more stable hydrogen bonding compared to amide groups of traditional PA layers, considerably enhancing the membrane's affinity for water molecule clusters.

Further validation was provided by radial distribution function (RDF) analysis (Fig. 5d). Within the first coordination shell, the RDF peak intensity for $-SO_3^-$–H_2O is significantly stronger than those for amide-H_2O and LDH-H_2O systems, corresponding to a coordination number of 1.84 (Supplementary Fig. 18). Additionally, the first peaks for $-SO_3^-$–H_2O and amide-H_2O are located at 0.27 nm and 0.28 nm, respectively, indicating a higher local density of water molecules around the oxygen atoms of $-SO_3^-$ groups and reflecting stronger interactions. Conversely, the gH–O (r) function for the LDH-H_2O system consistently remains below 1 within the hydrogen-bond cutoff radius, confirming that its interactions are primarily dominated by van der Waals forces. Collectively, these thermodynamic metrics elucidate the advantageous characteristics of the LDH-SL TFN membrane: by establishing abundant binding sites for water molecules, it significantly facilitates rapid transmembrane transport of water.

Discussion

This study unveils a previously unrecognized mechanism for the precise control of the structure and surface topology of the PA selective layer in TFN membranes. A strategy is developed using the organic-phase additive LDH-SL, whereby optimizing the doping ratio of SL achieves spatial manipulation of diffusion resistance, reducing bulk-phase transport while promoting the cross-interface diffusion of MPD monomers. This spatial manipulation induces fluctuations in the monomer diffusion rates and fluxes, ultimately resulting in heterogeneous polymerization dynamics. This breakthrough establishes a paradigm for the controllable fabrication of a thin and highly wrinkled PA layer in TFN membranes, which underpins the ultrafast water molecule kinetics observed. Furthermore, the LDH nanosheets, through van der Waals interactions with water molecules and a robust hydrogen-bonding network formed by the surface-modified $-SO_3^-$ groups interacting with water, significantly enhance the transmembrane transport kinetics of water molecules. The optimized 2LDH-1SL TFN membrane demonstrates exceptional separation performance, achieving a water permeability of 4.0 LMH bar^{-1} and maintaining a NaCl rejection rate of 99.4%, surpassing the performance of both state-of-the-art membranes reported in the literature and commercial TFC/TFN RO membranes. Notably, both the LDH and SL additives used in this study are environmentally compatible and cost-effective, fully aligning with green chemistry

https://doi.org/10.1038/s41467-025-64959-x

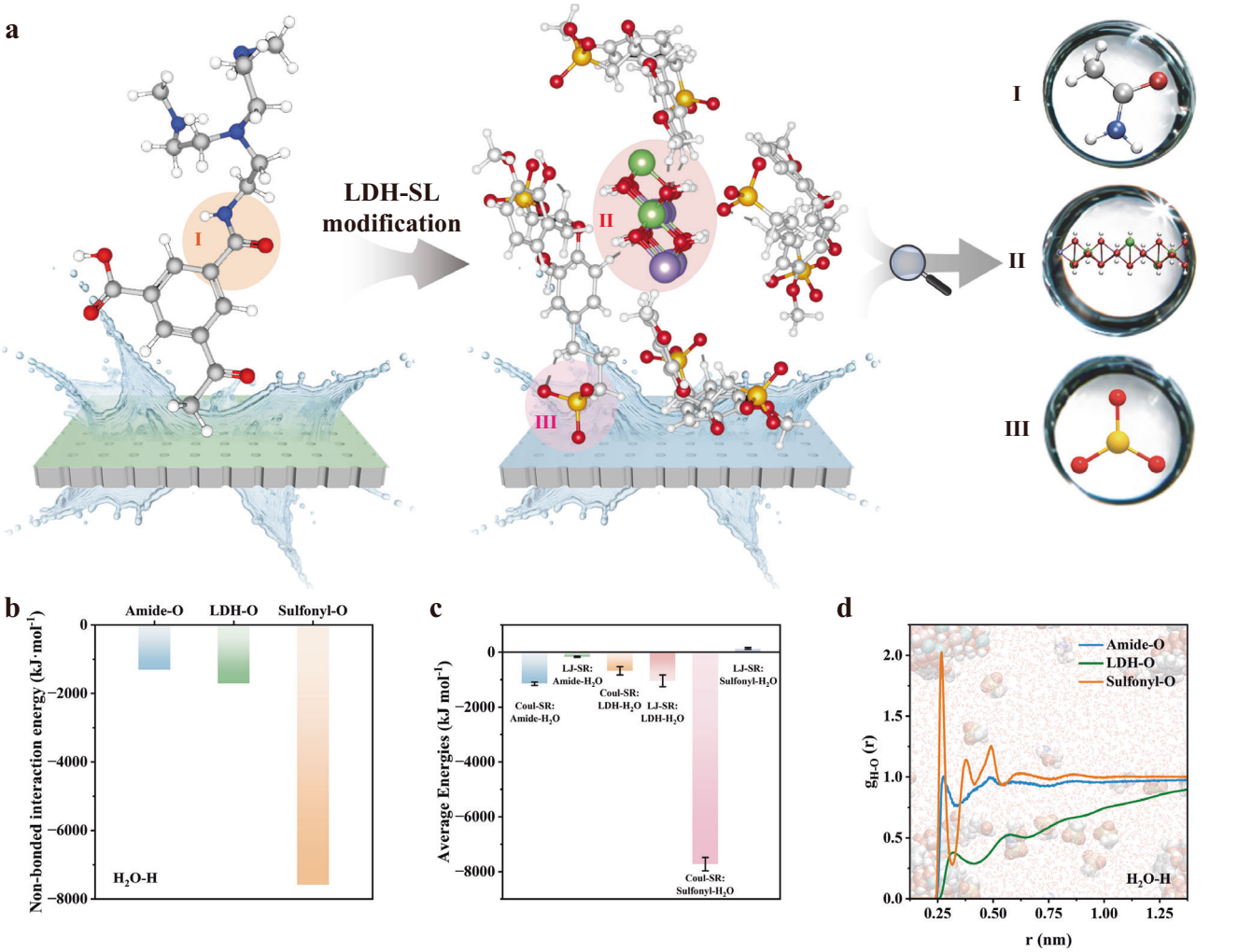

Fig. 5 | Mechanisms governing the incorporation of sodium lignosulfonate-modified layered double hydroxides (LDH-SL) nanoparticles in the fabrication of water permeation. a Three representative molecular fragments of the selectivity layer, with and without LDH-SL (left), accompanied by a schematic representation of the water cluster distribution in each fragment (right). **b** Non-bonded interaction energy (IE), along with **c** average energies—including Lennard-Jones short-range (LJ-SR) and Coulomb short-range (Coul-SR) interactions—between water molecules and fragments. Data are reported as mean values, with error bars representing the standard deviation over the simulation trajectory. **d** Radial distribution functions (RDF) between water molecules and fragments. All data and information presented in (**b**–**d**) are derived from molecular dynamics (MD) simulations.

principles and introducing no additional environmental burden throughout the ultrafast membrane fabrication process. These significant findings provide a crucial theoretical foundation and technical support for the design and production of next-generation RO membranes. Future work should focus on evaluating the long-term anti-fouling performance and operational stability under realistic feed water conditions to further validate practical applicability.

Methods

Materials and chemical reagents

Materials and chemical reagents can be found in Supplementary Experimental Methods 1.1.

Synthesis of LDH-SL nanoparticles

The pristine LDH was synthesized via a coprecipitation method. Briefly, a 100 mL aqueous solution containing 0.2 M Mg^{2+} and 0.1 M Al^{3+} was initially prepared. A 0.2 M Na_2CO_3 solution and a 1 M NaOH solution were subsequently added dropwise in equivalent volumes to the above solution until the pH reached approximately 10. The solution was then thermally aged at 70 °C for 20 h. Following this, the LDH precipitate was separated by centrifugation, washed twice with water and acetone, and redispersed in ethanol at a final concentration of 1 wt%. Acetone was utilized to improve the dispersibility of LDH in the organic phase during IP. For the synthesis of 2LDH-1SL, 0.125 g of SL was dissolved in 1 mL of ethanol and combined with 25 g of the LDH-ethanol solution, followed by vortexing for 2 min. The resulting 2LDH-1SL product was then recovered by centrifugation, washed with water and ethanol, and vacuum-dried at 60 °C overnight. The final product was stored in a sealed container for subsequent characterization and membrane fabrication.

Preparation of the LDH-SL TFN membrane

For the fabrication of the LDH-SL TFN membrane, polysulfone (PSF) substrates were initially immersed in a 2 wt% MPD aqueous solution containing 0.15 wt% sodium dodecyl sulfate (SDS) for 2 min. Subsequently, the excess solution was gently removed using a rubber roller with an effective area of 8 × 10 cm^2. The MPD-saturated substrates were then affixed to a plastic frame and exposed to a hexane/xylene (95/5 v/v) solution containing 0.15 wt% TMC and a specific concentration of 2LDH-1SL for 1 min. Prior to the IP process, the nanoparticles were incorporated into the organic monomer solution and agitated for 45 min. The resulting TFN membranes underwent thermal treatment at

80 °C for 4 min. For comparative purposes, a control TFC membrane was fabricated without the addition of nanoparticles, a control LDH TFN membrane was produced using pristine LDH nanofillers, and a control LDH-L TFN membrane was obtained using lignin-modified LDH nanofillers under identical conditions. All synthesized membranes were stored in deionized (DI) water at 5 °C for subsequent characterization and performance assessment.

Characterization of membranes

XRD (Bruker AXS D8, USA) and FTIR spectroscopy (Thermo Fisher-iS5, USA) were employed to analyze the chemical compositions of various nanomaterials. Transmission electron microscopy (TEM, Thermo Fisher Talos F200S, USA) was utilized to investigate the morphological characteristics of the nanoparticles. XPS (Thermo Scientific K-Alpha, USA) was applied to probe the chemical states of the surface compositions of the membranes. SEM (FEI NOVA 450, USA) was utilized to characterize both the surface and cross-sectional morphologies of the membranes. The membrane thickness was determined by measuring at a minimum of ten different locations from multiple cross-sectional SEM images for each sample, with the final value reported as the mean ± standard deviation. AFM (Bruker Dimension ICON, USA) was employed to assess the surface roughness of the membranes. The WCAs and interfacial tension were measured using a goniometer (Dataphysics DCAT21, Germany) following the sessile drop method. The FFV and pore size of the membranes were evaluated using PALS.

Reverse osmosis performance tests

To evaluate the separation performance of membranes, cross-flow filtration equipment with an operational area of 15 cm^2 was utilized. Prior to the collection of permeate samples, all membranes were precompacted for 30 min. Unless otherwise specified, the applied pressure, cross-flow velocity, and feed solution temperature were maintained at 15 bar, 1 L min^{-1}, and 25 °C, respectively. The water permeance (A, LMH bar^{-1}), salt rejection (R, %), and salt permeability (B, LMH) were determined using a feed solution containing 2000 ppm NaCl, as calculated by Eqs. (1–4):

$$J_w = \frac{\Delta V}{\Delta t \times S} \tag{1}$$

$$A = \frac{J_w}{\Delta p - \Delta \pi} \tag{2}$$

where J_w is the water flux (LMH), ΔV (L) is the volume of permeate collected over the time interval Δt (h), S (m^2) is the effective filtration area of the membrane, ΔP (bar) is the pressure differential across the membrane, and $\Delta \pi$ (bar) is the osmotic pressure differential across the membrane.

$$R = \left(1 - \frac{C_p}{C_f}\right) \times 100\% \tag{3}$$

$$B = \left(\frac{1}{R} - 1\right) \times J_w \tag{4}$$

where Cp and Cf are the salt concentrations in the permeate and feed solution, respectively. The salt concentration was determined by measuring the conductivity using a DDSJ-307F (Shanghai Rex) conductivity meter.

MD simulations

All MD simulations were conducted using the GROMACS 2021 software package[61–63]. The bonded and non-bonded interactions of Mg and Al atomic structures were modeled utilizing the Universal Force Field. The molecular geometries of *n*-hexane and MPD were initially optimized using Gaussian 16 software[64] and subsequently characterized using the General Amber Force Field, incorporating parameters from the AuToFF web server[65] and employing the RESP charge model[66]. Electrostatic interactions were computed via the Particle-Mesh Ewald method, with a cutoff distance of 1.6 nm applied for short-range van der Waals interactions[67]. To investigate the trans-interface resistance of MPD, the free energy required for its transport through the water/hexane interface was determined using a combination of umbrella sampling and the weighted histogram analysis method. Two primary simulated systems were constructed: one comprising a water/hexane system and another incorporating 2LDH-1SL into the water/hexane framework. Both systems were simulated within an NVT thermodynamic ensemble at a temperature of 298 K. The simulation cells comprised 4000 H_2O molecules and 10 MPD molecules in the aqueous phase, along with 700 hexane molecules in the organic phase, with periodic boundary conditions implemented in all directions. For the umbrella sampling procedure, the simulation cell was divided into multiple sampling segments along the transport coordinate, with each segment measuring 0.5 Å in length. During the MD process, one MPD molecule was initially fixed at the center of each sampling segment using a harmonic spring potential with an elastic coefficient of 3000 kJ mol^{-1} nm^{-2}. Each segment was then simulated for 10,000,000 steps, with each step lasting 1 fs (resulting in a total simulation time of 10 ns per window), to achieve the final equilibrium state. Simulations intended to calculate interaction energies and RDF were performed in separate, smaller simulation boxes containing water and specific molecular fragments of interest to ensure adequate statistical sampling. The uncertainty in the final potential of mean force profiles and the interaction energies was calculated as the standard deviation over the simulation trajectory.

Data availability

All data in the manuscript or the supplementary information are available from the corresponding authors upon request. Source data are provided with this paper.

References

1. Shannon, M. A. et al. Science and technology for water purification in the coming decades. *Nature* **452**, 301–310 (2008).
2. Gin, D. L. & Noble, R. D. Designing the next generation of chemical separation membranes. *Science* **332**, 674–676 (2011).
3. Elimelech, M. & Phillip, W. A. The future of seawater desalination: energy, technology, and the environment. *Science* **333**, 712–717 (2011).
4. Chen, L. et al. Ion sieving in graphene oxide membranes via cationic control of interlayer spacing. *Nature* **550**, 380–383 (2017).
5. Joshi, R. K. et al. Precise and ultrafast molecular sieving through graphene oxide membranes. *Science* **343**, 752–754 (2014).
6. Lu, G. et al. Nano-confined controllable crystallization in supramolecular polymeric membranes for ultra-selective desalination. *Nat. Commun.* **16**, 2284 (2025).
7. Hinds, B. J. et al. Aligned multiwalled carbon nanotube membranes. *Science* **303**, 62–65 (2004).
8. Yang, Y. et al. Large-area graphene-nanomesh/carbon-nanotube hybrid membranes for ionic and molecular nanofiltration. *Science* **364**, 1057–1062 (2019).
9. Park, H. B., Kamcev, J., Robeson, L. M., Elimelech, M. & Freeman, B. D. Maximizing the right stuff: the trade-off between membrane permeability and selectivity. *Science* **356**, eaab0530 (2017).
10. Sarkar, P., Modak, S. & Karan, S. Ultraselective and highly permeable polyamide nanofilms for ionic and molecular nanofiltration. *Adv. Funct. Mater.* **31**, 2007054 (2021).
11. Di, J. W. et al. Recent progress in advanced polyamide nanofiltration membranes via interfacial polymerization for desalination and beyond. *Desalination* **592**, 118167 (2024).

12. Morgan, P. W. Condensation polymer: by interfacial and solution methods. *J. Soc. Dye. Colour.* **10**, 259 (1965) .
13. Freger, V. Kinetics of film formation by interfacial polycondensation. *Langmuir* **21**, 1884–1894 (2005).
14. Freger, V. Nanoscale heterogeneity of polyamide membranes formed by interfacial polymerization. *Langmuir* **19**, 4791–4797 (2003).
15. Liu, S., Wu, C., Hung, W.-S., Lu, X. & Lee, K.-R. One-step constructed ultrathin Janus polyamide nanofilms with opposite charges for highly efficient nanofiltration. *J. Mater. Chem. A* **5**, 22988–22996 (2017).
16. Zhang, Y. et al. Ice-confined synthesis of highly ionized 3D-quasilayered polyamide nanofiltration membranes. *Science* **382**, 202–206 (2023).
17. An, X. et al. The permeability-selectivity of polyamide-based membranes: role of ambient temperature in the interfacial polymerization. *Environ. Sci. Technol. Lett.* **11**, 1129–1135 (2024).
18. Wang, Z. et al. Nanoparticle-templated nanofiltration membranes for ultrahigh performance desalination. *Nat. Commun.* **9**, 2004 (2018).
19. Zhu, X. et al. Ultrathin thin-film composite polyamide membranes constructed on hydrophilic poly(vinyl alcohol) decorated support toward enhanced nanofiltration performance. *Environ. Sci. Technol.* **54**, 6365–6374 (2020).
20. Yang, Z. et al. Tannic acid/Fe^{3+} nanoscaffold for interfacial polymerization: toward enhanced nanofiltration performance. *Environ. Sci. Technol.* **52**, 9341–9349 (2018).
21. Jiang, C. et al. Thin-film composite membranes with aqueous template-induced surface nanostructures for enhanced nanofiltration. *J. Membr. Sci.* **589**, 117244 (2019).
22. Chowdhury, M. R., Steffes, J., Huey, B. D. & McCutcheon, J. R. 3D printed polyamide membranes for desalination. *Science* **361**, 682–686 (2018).
23. Li, Z., Zhao, F., Chen, H., Yang, L. & Zhang, J. 3D electrospray printing PEI-TMC nanofiltration membrane for efficient and long-term stable separation of Mg^{2+}/Li^{+}. *J. Membr. Sci.* **713**, 123373 (2025).
24. Wen, Y. et al. Metal-organic framework enables ultraselective polyamide membrane for desalination and water reuse. *Sci. Adv.* **8**, eabm4149 (2022).
25. Zhao, C. et al. Polyamide membranes with nanoscale ordered structures for fast permeation and highly selective ion-ion separation. *Nat. Commun.* **14**, 1112 (2023).
26. Zhang, Y. Q. et al. Engineering covalent organic framework membranes for efficient ionic/molecular separations. *Matter* **7**, 1406–1439 (2024).
27. Liu, M.-L. et al. Evolution of functional nanochannel membranes. *Prog. Mater. Sci.* **139**, 101162 (2023).
28. Ge, M. et al. Impact of graphitic carbon nitride/polydopamine on permeance and antifouling performance of reverse osmosis membranes. *Sep. Purif. Technol.* **360**, 130949 (2025).
29. Werber, J. R., Osuji, C. O. & Elimelech, M. Materials for next-generation desalination and water purification membranes. *Nat. Rev. Mater.* **1**, 16018 (2016).
30. Sheng, K. et al. Three-dimensional covalent organic frameworks for advanced membrane separations. *Adv. Membr.* **4**, 100109 (2024).
31. Li, X. et al. A novel high temperature resistance thin film composite polyamide reverse osmosis membrane with covalent organic frameworks intermediate layer. *Adv. Membr.* **4**, 100101 (2024).
32. Hao, Y. et al. An ultrahighly permeable-selective nanofiltration membrane mediated by an in situ formed interlayer. *J. Mater. Chem. A* **8**, 5275–5283 (2020).
33. Ji, C. et al. Recent advances in high-performance TFC membranes: a review of the functional interlayers. *Desalination* **500**, 114869 (2021).
34. Li, W.-L. et al. High-performance thin-film composite (TFC) membranes with 2D nanomaterial interlayers: an overview. *Results Eng.* **21**, 101932 (2024).
35. Song, F. & Hu, X. Exfoliation of layered double hydroxides for enhanced oxygen evolution catalysis. *Nat. Commun.* **5**, 4477 (2014).
36. Zhao, Q. et al. Thin-film nanocomposite membranes with polyol-functionalized layered double hydroxides for boron removal via reverse osmosis. *J. Membr. Sci.* **695**, 122497 (2024).
37. Karan, S., Jiang, Z. & Livingston, A. G. Sub–10 nm polyamide nanofilms with ultrafast solvent transport for molecular separation. *Science* **348**, 1347–1351 (2015).
38. Shen, L. et al. Polyamide-based membranes with structural homogeneity for ultrafast molecular sieving. *Nat. Commun.* **13**, 500 (2022).
39. Liang, Y. et al. Polyamide nanofiltration membrane with highly uniform sub-nanometre pores for sub-1 Å precision separation. *Nat. Commun.* **11**, 2015 (2020).
40. Tan, Z., Chen, S., Peng, X., Zhang, L. & Gao, C. Polyamide membranes with nanoscale Turing structures for water purification. *Science* **360**, 518–521 (2018).
41. Zhang, W. et al. Lignin alkali regulated interfacial polymerization towards ultra-selective and highly permeable nanofiltration membrane. *Nat. Commun.* **16**, 371 (2025).
42. Deng, Y., Zhang, Q. & Qu, D.-H. Emerging hydrogen-bond design for high-performance dynamic polymeric materials. *ACS Mater. Lett.* **5**, 480–490 (2023).
43. Putz, K. W., Compton, O. C., Palmeri, M. J., Nguyen, S. T. & Brinson, L. C. High-nanofiller-content graphene oxide–polymer nanocomposites via vacuum-assisted self-assembly. *Adv. Funct. Mater.* **20**, 3322–3329 (2010).
44. Wang, Q., Tay, H. H., Zhong, Z., Luo, J. & Borgna, A. Synthesis of high-temperature CO_2 adsorbents from organo-layered double hydroxides with markedly improved CO_2 capture capacity. *Energy Environ. Sci.* **5**, 7526–7530 (2012).
45. Guo, W. et al. Mismatching integration-enabled strains and defects engineering in LDH microstructure for high-rate and long-life charge storage. *Nat. Commun.* **13**, 1409 (2022).
46. Iqbal, W. et al. Parametric and non-parametric spectral signal processing techniques for estimation of periodicity in sunspot numbers. *Proc. Pak. Acad. Sci.* **56**, 9–20 (2019).
47. Wang, B., Zhang, H., Evans, D. G. & Duan, X. Surface modification of layered double hydroxides and incorporation of hydrophobic organic compounds. *Mater. Chem. Phys.* **92**, 190–196 (2005).
48. Zhang, G. et al. Growth behavior of MgAl-layered double hydroxide films by conversion of anodic films on magnesium alloy AZ31 and their corrosion protection. *Appl. Surf. Sci.* **456**, 419–429 (2018).
49. Liu, C. et al. Effect of sodium lignosulfonate on bonding strength and chemical structure of a lignosulfonate/chitosan-glutaraldehyde medium-density fiberboard adhesive. *Adv. Compos. Hybrid. Mater.* **4**, 1176–1184 (2021).
50. Shao, S. et al. Nanofiltration membranes with crumpled polyamide films: a critical review on mechanisms, performances, and environmental applications. *Environ. Sci. Technol.* **56**, 12811–12827 (2022).
51. Wong, M. C. Y., Lin, L., Coronell, O., Hoek, E. M. V. & Ramon, G. Z. Impact of liquid-filled voids within the active layer on transport through thin-film composite membranes. *J. Membr. Sci.* **500**, 124–135 (2016).
52. Culp, T. E. et al. Nanoscale control of internal inhomogeneity enhances water transport in desalination membranes. *Science* **371**, 72–75 (2021).
53. Lai, G. S. et al. Tailor-made thin film nanocomposite membrane incorporated with graphene oxide using novel interfacial polymerization technique for enhanced water separation. *Chem. Eng. J.* **344**, 524–534 (2018).

54. Zhang, C. et al. Molecular dynamics insights into water transport mechanisms in polyamide membranes: Influence of cross-linking degree. *J. Phys. Chem. B* **129**, 1697–1706 (2025).
55. Lu, Z. et al. Loosely nanostructured polyamide membranes with rapid water transport for efficient molecule/ion separation. *J. Membr. Sci.* **722**, 123901 (2025).
56. Gan, Q. et al. Nanofoamed polyamide membranes: mechanisms, developments, and environmental implications. *Environ. Sci. Technol.* **58**, 20812–20829 (2024).
57. Zheng, F. et al. High-performance nanofiltration membrane with dual resistance to gypsum scaling and biofouling for enhanced water purification. *Environ. Sci. Technol.* **58**, 16656–16668 (2024).
58. Hu, Y., Wang, F., Yang, Z. & Tang, C. Y. Modeling nanovoid-enhanced water permeance of thin film composite membranes. *J. Membr. Sci.* **675**, 121555 (2023).
59. Yu, M., Foster, A. B., Kentish, S. E., Scholes, C. A. & Budd, P. M. Recent progress in thin film composite membranes based on the polymer of intrinsic microporosity PIM-1: Preparation, properties and performance. *J. Membr. Sci.* **722**, 123844 (2025).
60. Wang, W., Jin, Y., Meng, X., Yang, N. & Zhu, X. Dynamic short hydrogen-bonding network enhancing hydrophilicity in biomimetic membranes with artificial water channels for efficient removal of dyes and salts. *Angew. Chem. Int. Ed.* **64**, e202502204 (2025).
61. Van Der Spoel, D. et al. GROMACS: fast, flexible, and free. *J. Comput. Chem.* **26**, 1701–1718 (2005).
62. Abraham, M. J. et al. GROMACS: High performance molecular simulations through multi-level parallelism from laptops to supercomputers. *SoftwareX* **1-2**, 19–25 (2015).
63. Berendsen, H. J. C., van der Spoel, D. & van Drunen, R. GROMACS: a message-passing parallel molecular dynamics implementation. *Comput. Phys. Commun.* **91**, 43–56 (1995).
64. Gaussian 16 Rev. C.01. https://gaussian.com/citation/ (Wallingford, CT, 2016).
65. Wang, C. L. et al. AuToFF Program, Vesrion 1.0. Hzwtech. Shanghai, https://cloud.hzwtech.com/web/product-service?id=36 (2023).
66. Bayly, C. I., Cieplak, P., Cornell, W. & Kollman, P. A. A well-behaved electrostatic potential based method using charge restraints for deriving atomic charges: the RESP model. *J. Phys. Chem.* **97**, 10269–10280 (1993).
67. Darden, T., York, D. & Pedersen, L. Particle mesh Ewald: an N·log(N) method for Ewald sums in large systems. *J. Chem. Phys.* **98**, 10089–10092 (1993).

Acknowledgements

This work is financially supported by the National Natural Science Foundation of China (No. 52270076, 92475205, 22178076), the National Key R&D Program (2023YFE0127000), and the Open Research Fund of Suzhou Laboratory (No. SZLAB-1308-2024-ZD007). Prof. Zhao would also like to thank the financial aid from the Fundamental Research Funds for the Central Universities (22120250217).

Author contributions

Q.P.Z. and R.Y.L. conceived the initial idea and experimental design. R.Y.L. conducted the experiments and drafted the original manuscript. F.F. performed the PALS characterization and analysis. Q.P.Z., H.Q.C., Y.L.Z., X.J. and L.S. supervised the study and experiments. X.F.Z., H.Q.C., L.S. and Y.L.Z. provided funding for the project. All authors contributed to both the drafting and revising of the manuscript.

Competing interests

The authors declare no competing interests.

Additional information

Supplementary information The online version contains supplementary material available at https://doi.org/10.1038/s41467-025-64959-x.

Correspondence and requests for materials should be addressed to Huaqiang Chu, Xu Jiang, Lu Shao or Yalei Zhang.

Peer review information *Nature Communications* thanks Zak Hughes, Jie Shen, and the other anonymous reviewer(s) for their contribution to the peer review of this work. A peer review file is available.